Konstantinos P. Baxevanakis

First   *Last*

*VOR (version of record)

Data-driven Damage Model based on Nondestructive Evaluation

Konstantinos P. Baxevanakis[1], Brian Wisner[2], Sara Schlenker[2], Harsh Baid[3],
and Antonios Kontsos[2,*]

[1]*Wolfson School of Mechanical, Electrical and Manufacturing Engineering,
Loughborough University, LE11 3TU, UK*
[2]*Theoretical & Applied Mechanics Group, Mechanical Engineering & Mechanics Department,
Drexel University, 3141 Chestnut Street, Philadelphia, PA 19104*
[3]*AlphaSTAR Corporation, 5150 East Pacific Coast Highway, Long Beach, CA 90804*

*Corresponding author: antonios.kontsos@drexel.edu, (215) 895 2297

Abstract: A computational damage model which is driven by material, mechanical behavior and nondestructive evaluation data is presented in this study. To collect material and mechanical behavior damage data, an aerospace grade precipitate-hardened aluminum alloy was mechanically loaded under monotonic conditions inside a Scanning Electron Microscope, while acoustic and optical methods were used to track the damage accumulation process. In addition, to obtain experimental information about damage accumulation at the laboratory scale, a set of cyclic loading experiments was completed using 3-point bending specimens made out of the same aluminum alloy and by employing the same nondestructive methods. The ensemble of recorded data for both cases was then used in a post-processing scheme based on outlier analysis to form damage progression curves which were subsequently used as custom damage laws in finite element simulations. Specifically, a plasticity model coupled with stiffness degradation triggered by the experimentally defined damage curves was used in custom subroutines. The results highlight the effect of the data-driven damage model on the simulated mechanical response of the geometries considered and provide an information workflow that is capable of coupling experiments with simulations that can be used for remaining useful life estimations.

Keywords: Data-driven model, Damage Mechanics, Acoustic emission, Digital Image Correlation, Remaining Useful Life

1. Introduction

Damage is a multiscale, spatially distributed, stochastic process bridging nucleation and growth that varies significantly among different material types. The damage process spans four distinct stages including incubation, microstructurally-small initiation, physically small growth and extensive growth processes [1, 2]. In fact, it has been reported that the incubation, nucleation and microstructurally-small growth regions consume most of the material's life particularly in high cycle fatigue loading schemes [1]. During this significant portion of material life, local microstructural features, which for example in metals include grain size and orientations, inclusions, voids etc. play a dominant role which might not be detrimental, however, it may lead to conditions that favor the subsequent development of known catastrophic failure modes such as cracks. From an engineering perspective, this fact has been recently leveraged by investigating innovative sensing methods [3-5], as well as new materials design approaches [6] in order to make a transition from damage monitoring to damage precursor identification and understanding [7-10].

Damage models discussed in the literature generally focus on defining material degradation due to damage using phenomenological approaches that target the analytical description of the particular role of individual mechanisms. In several cases, a damage variable, D, is defined as the ratio between the damaged and the total area of a reference volume. If damage is isotropic a scalar damage variable is defined; anisotropic damage leads to the adoption of a second order damage tensor. The damage parameter has a value of zero in the undamaged state and a value of one when final material failure has occurred [11]. In this context, Kuna and Wippler [12] used a unified Chaboche model derived from a free energy potential which was enhanced to account for void

2

growth. A thermodynamic approach was used in Richard et al. [13] to model damage in quasi-brittle materials. Other efforts have brought a more physics-based approach to the definition of damage. For example, Liu and Zheng [14] provided a review of damage modeling techniques in composite laminates including the use of phenomenological damage tensors in continuum damage models and multiscale finite element methods that derive their damage parameters via stochastic analysis of the underlying micro-mechanisms. Moreover, Rinaldi et al. [15] introduced a microstructure-aware damage parameter in two-dimensional lattice models that is related to the coherence length between microcracks. For an overview of microstructure-sensitive computational models with an application to fatigue crack growth, the authors refer to McDowell and Dunne [1] and references therein.

Several characterization and experimental methods have been employed to quantitatively monitor damage from microscale samples [4, 16-22] to full scale structures [23, 24]. In the case of precipitate-hardened alloys which is the material used in this article, damage has been reported to initiate at intermetallic inclusions resulting from the alloying process which lead to early crack nucleation followed by growth [25, 26]. In addition to image-based characterization, nondestructive evaluation (NDE) techniques have been proven useful in monitoring the damage processes at the material level. For example, Digital Image Correlation (DIC) methods are currently routinely used in experimental mechanics to track full field deformations; localizations observed in such datasets have been successfully linked to ductile fracture [24, 27], twinning [19, 28-30], and particle fracture [4, 31-33]. Additionally, Acoustic Emission (AE) has proven useful in detecting microscale damage such as dislocation motion and particle fracture [4, 34, 35], as well as macro scale damage such as

crack growth [27, 36-40]. Additional NDE methods reported to monitor material damage including infrared thermography [41-43], electromechanical impedance [44-46] and ultrasonic testing [47-49].

By combining experimental and simulation methods a different class of data-driven damage models has been reported. For example Barbero, Abdelal and Caceres [50] proposed a second order damage tensor that is formed and evolved with model parameters defined through experimental data. In addition, Kompalka, Reese and Bruhns [51] used successive model updating to refine an initial polynomial approximation of a damage parameter used to define the damage evolution at a number of integration points in FEM simulations. Moreover, Zárate et al. [52] predicted fatigue crack growth from AE data in a probabilistic model that provides predictions of the stress intensity factor. More recently, Loutas et al. [53] used a machine learning protocol to incorporate AE data features into a damage model for composites that is agnostic to the particular damage mechanisms for the specific material used in experiments.

Given this state of the art, this article presents a novel damage model that leverages micro-structural level material information along with mechanical behavior and NDE data to define damage evolution curves. A computational workflow is then developed to use such data-defined damage information into simulations of both monotonic and cyclic behavior.

2. Experimental and Computational Approach

2.1 Material Characterization Data

An aerospace grade precipitate-hardened aluminum alloy, Al 7075-T6351, rolled to 2.5 mm thickness was used in the as-received condition. The primary alloying element is Zinc (6.1-6.1%) with traces of Silicon (0.4%), Iron (0.5%), Copper, (1.2-2.0%), Manganese (0.3%), Magnesium (2.1-2.9%), and

Chromium (0.18-0.28%) according to literature [54] and verified by Energy Dispersive Spectroscopy (EDS). The addition of these elements increases the yield and ultimate strength of the material, however, these same strengthening elements have been shown to be nucleation points of damage [4, 55], particularly at the larger particles that form from the alloying process [2, 56]. A Scanning Electron Microscope (FEI XL30 ESEM) equipped with an EDAX Electron Backscatter Diffraction (EBSD) camera was used to obtain the microstructural information shown in Fig.1. The data plotted in Fig. 1a-b reveal a nearly equiaxed grain structure with an average grain size of 60 µm. The presence of a rolling texture was also observed in the pole figures in Fig. 1c where the [100] axis is aligned with the rolling direction in a 1.5 x 1.5 mm^2 area.
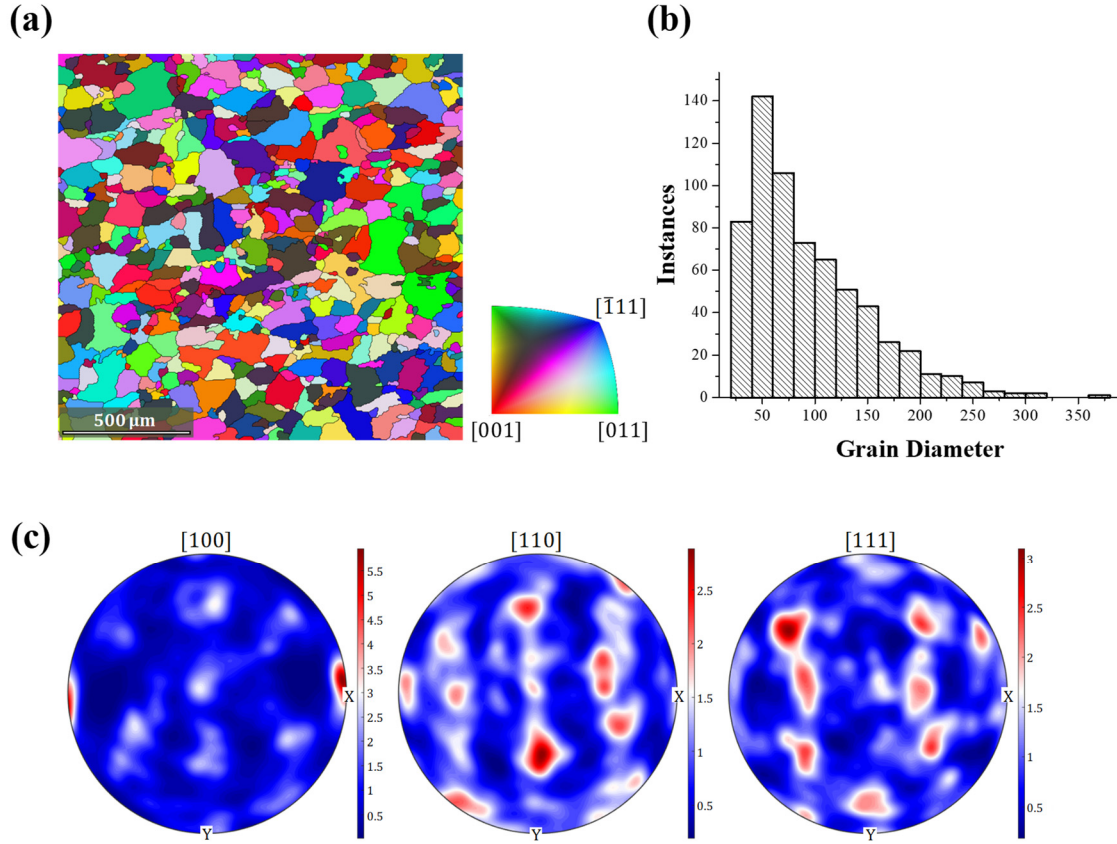

Fig. 1: Texture information: (a) Inverse pole figure map showing predominantly equiaxed grains, (b) histogram showing grain size distribution, and (c) pole figure revealing a rolling texture.

Experiments were conducted using a micro-tensile stage (GATAN) capable of applying up to 2100N inside an SEM microscope as shown in Fig. 2a and 2b. Additionally, NDE data including full field strain and acoustic emission activity were recorded similar to previous work by the authors [4, 5]. Specifically, AE monitoring was achieved inside the SEM microscope by use of a BNC (Bayonet Neill–Concelman) pass-through on the custom SEM load stage door shown in Fig. 2a. In this investigation, two broadband PICO sensors with a frequency range from approximately 150 to 750kHz, shown in Fig. 2c, were used. The sensor frequency response is shown in Fig. 2d. Signals were recorded from the sensors with a sampling rate of 10 million samples per second using a peak definition, hit definition, and hit lock out time of 100, 500, and 500 μs, respectively. A 25 dB threshold was used for the test based on eliminating ambient signals collected while no load was applied. Fig. 3 shows the specimen geometry used which has a reduced area gage section to ensure the specimen fractures inside the monitored region, while providing sufficient space to attach the AE sensors.

The 1.3 x 2.5 x 3 mm gage section ensures that there are approximately 10,000 grains in the gage and 200 grains in the cross section which is sufficient to obtain the bulk material behavior. Prior to testing, specimens were ground and polished to a 0.05 μm surface finish to minimize the effects of surface defects in the damage evolution of the material. In addition, ink toner, with speckle size of approximately 8 μm, was applied to the surface to provide sufficient contrast for DIC imaging in a Field of View (FOV) of 1.3 x 2.5 mm, which indicated by the gray field in the center of the specimen in Fig. 3. The specimen was then loaded at a rate of 0.1 mm/min until failure while images

were captured via live video monitoring using a 4-frame average at 30 frames per second. Fig. 4a shows the load versus measured axial strain curve along with full field deformation maps at the 6 locations marked in Fig. 4a.
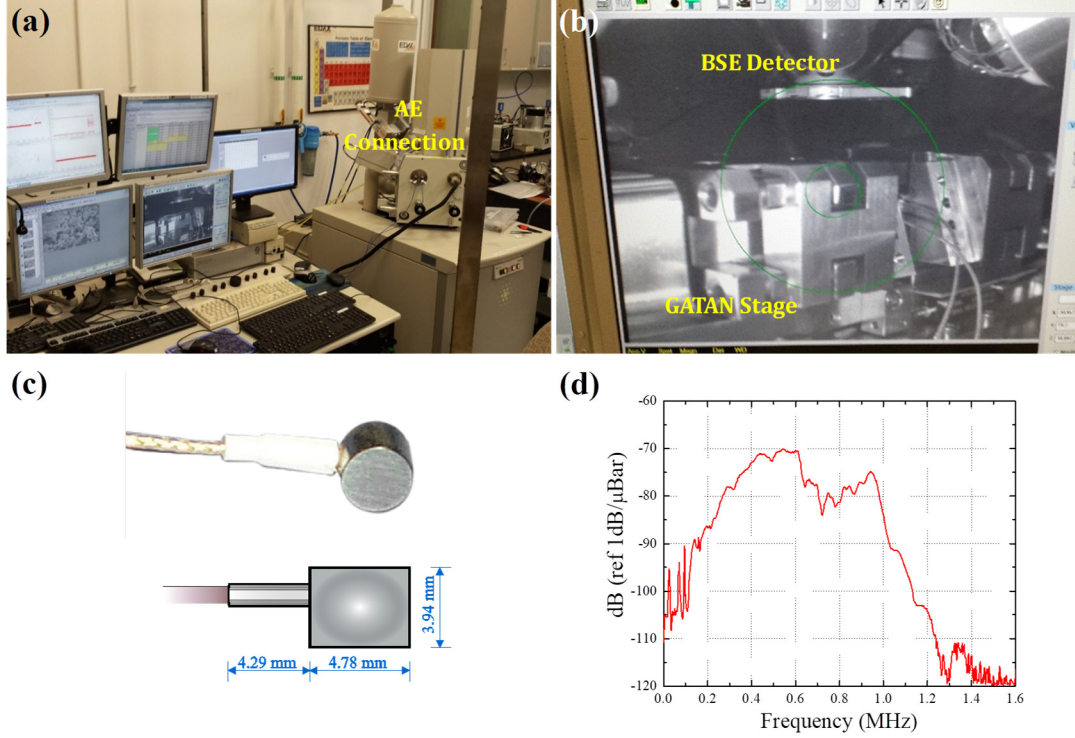

Fig. 2: (a) Mechanical and nondestructive test setup in a FEI XL30 SEM, (b) GATAN Stage inside the SEM showing the BSE Detector, (c) PICO Sensor used for AE monitoring, (d) PICO sensor frequency response.

In order to obtain experimental information in a fatigue setting, a set of cyclic loading experiments was also completed. For these experiments, a prismatic beam of dimensions $200{\times}50{\times}19$ mm was loaded under 3-point bending tensile cyclic conditions ($R = 0.1$) for 50 cycles. During the experiment, AE and DIC information was collected and a similar procedure to the monotonic case was followed.
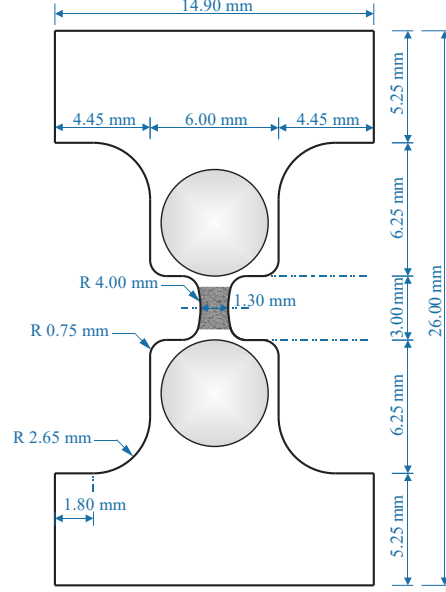
Fig. 3: Hourglass-type specimen dimensions and placement of the acoustic emission sensors. The shaded area indicates the FOV for DIC measurements.
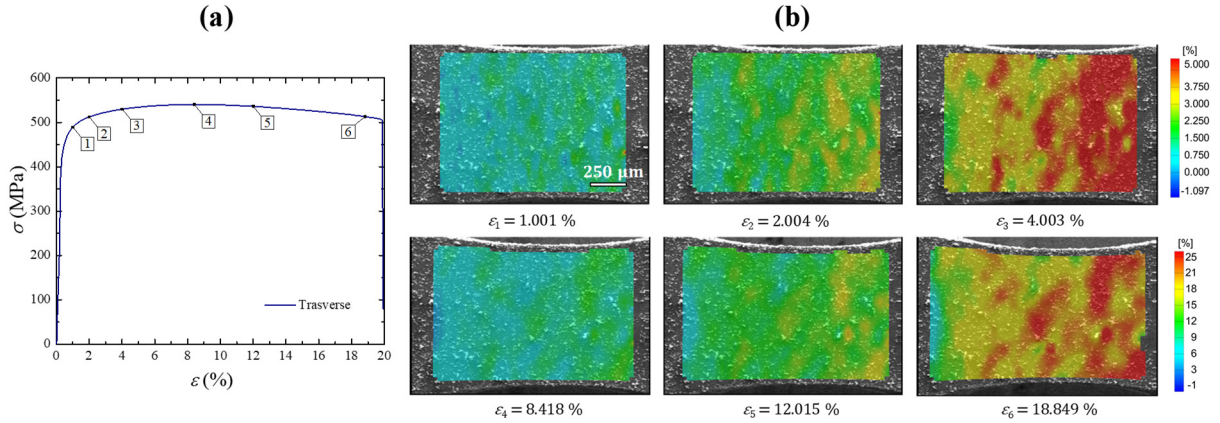

Fig. 4: (a) DIC snapshots in the macroscopic stress-strain response curve, (b) strain evolution in the monitored by DIC region.

2.3 Acoustic Emission data and microstructural evidence

Real time recorded AE activity was passed through a frequency filter that matched the range of the sensors. Thirty-two AE features were extracted; selected AE features were correlated with the load in Fig. 5, revealing a spike of AE activity at the onset of yielding. Fig. 5a shows that most of the recorded AE signals have amplitudes below 40dB with the exception of the activity near the yielding

point and the final failure of the specimen. Further, a clear distinction between signals with higher peak frequencies, above 400 kHz, and lower peak frequencies, below 200 kHz, is observed in Fig. 5b. Further, the amount of energy within the higher frequency range (400-600 kHz) called Partial Power 3, is shown in Fig. 5c to be decaying after yielding. This observation agrees with the trends seen in Fig. 5d where the majority of count activity happens around the yield point where the cumulative hits and energy start to increase. Specifically, the energy appears to instantly jump at yielding while the hits gradually increase.

Examining the specimen post mortem allows for the identification of damage mechanisms as shown previously by the authors [4, 27, 37] such as cracking and particle fracture. Specifically, Fig. 6 shows the presence of several damage mechanisms observed by ex-situ microscopy and while the specimen was still in the load frame inside the SEM both near, (i.e. within 1mm) and further away (further than 1mm) from the crack tip. These micro mechanisms which include precipitate fracture, microcracks and slip lines are possibly related to the large amount of AE activity, particularly, the higher amplitude hits in Fig. 5a and the jump in AE energy in Fig 5d that appear at the onset of yielding.
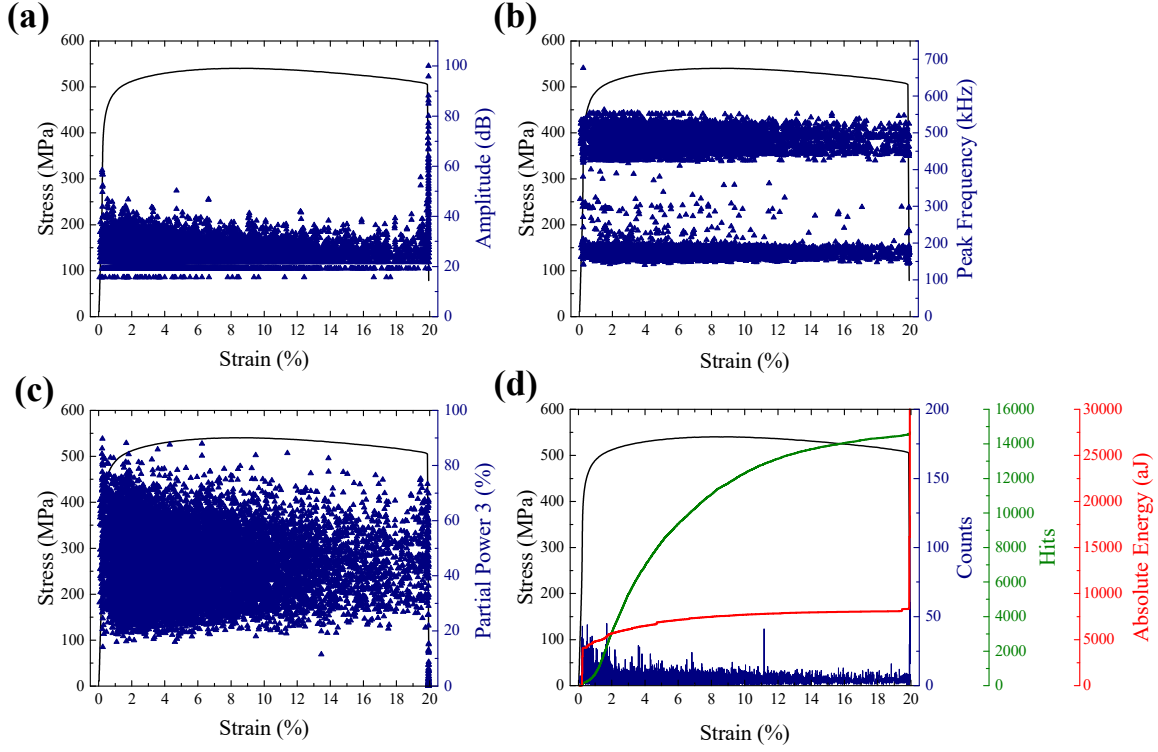
Fig. 5: Acoustic emission features plotted for the entire duration of the *in-situ* tension test: (a) amplitude, (b) peak frequency, (c) partial power 3, (d) counts, cumulative hits, and cumulative absolute energy.
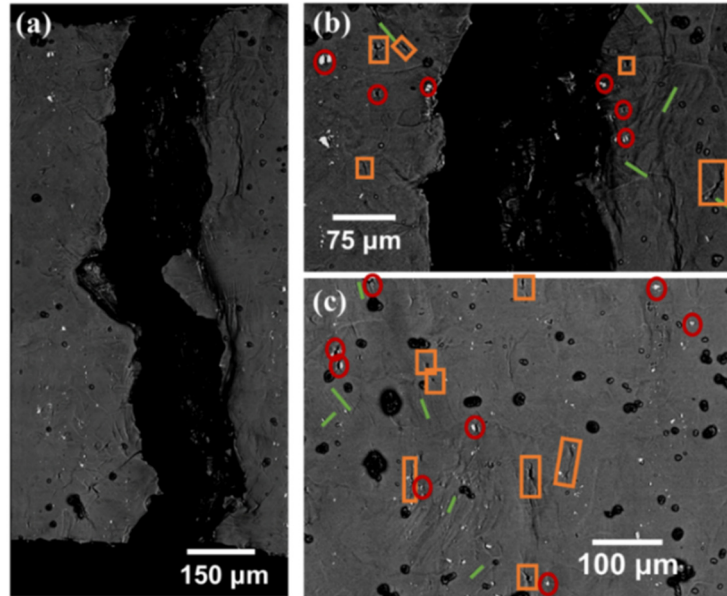

Fig. 6: (a) Post-mortem SEM image of the crack, microdamage identification near the crack (b) and away from the crack (c) in the forms of precipitate fracture (red), micro-cracks (red) and slip lines (green).

A normalized subset of the extracted AE features was determined by using the correlation and variance within all 32 features available. A complete list of the available AE features that can be extracted in recorded AE activity and their definition is given in ASTM E1316-17a. The correlation between each feature and all others used the data from the experiment and a correlation matrix. The mean correlation value for each feature was then calculated and the features with the lowest values below a correlation value of 0.25 where selected. Choosing the least correlated features ensures that most of the information in the recorded AE signals is preserved while using the smallest number of features to parametrically represent them. In this case, 5 features (namely the decay angle, re-verberation frequency, initiation frequency, FFT peak frequency, and peak frequency) were deter-mined to be sufficient to represent the AE data.

A damage curve was then generated from the AE data using an outlier analysis based on the Mahalanobis Squared Distance (MSD) formally defined as

$$D_M = \left(\mathbf{X} - \boldsymbol{\mu} \right)^T \mathbf{S}^{-1} \left(\mathbf{X} - \boldsymbol{\mu} \right) \tag{1}$$

where $\mathbf{X}$ is, in this case, a n x 5 matrix where each column represents each feature and each row represents a single AE signal, $\mathbf{S}$ is the covariance matrix of the feature values and $\boldsymbol{\mu}$ is defined as the baseline defined by noise AE signals (i.e. by using those signals recorded before loading was applied). The diagonal of the resulting matrix represents the MSD value and the normalized in a scale between 0 and 1 cumulative sum of all the points produces the damage curve shown in Fig. 7, which is plotted as a function of the to the specimen's life fraction defined using the total strain reached in the experiments. Interestingly, the MSD curve presents a sharp increase near the onset

of the plateau region in the stress-strain curve of Fig. 7 while it continues to grow with a decreasing rate until final failure. It should be noted also that at peak stress the MSD shows a ~60% remaining useful life (RUL) demonstrating that this parameter can provide a quantitative way to estimate it based on input data from the NDE setup. Furthermore, the fact that the MSD curve was defined as a function of measured strain allows its connection to model parameters as explained next.
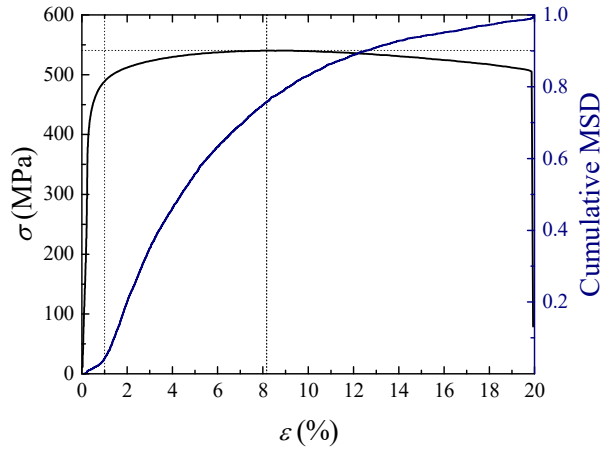

Fig. 7: Cumulative MSD for monotonic Al 7075 specimens taken from the transverse direction during in-situ experiments.

The same procedure used to examine the AE and DIC data for the in situ monotonic tension case was used to process the data obtained during the 3-pt bending fatigue test. Fig. 8 shows the raw AE data in the form of amplitude, peak frequency, cumulative hits and cumulative energy overlaid with the evolution of the maximum longitudinal strain value observed by DIC. Similar behavior occurs in this condition as for the in situ monotonic loading case where a concentration of hits with peak frequencies above 400 kHz occurring early in the specimen's life and decaying as more cycles are applied. A similar trend is observed in amplitude while the cumulative hits and absolute energy show a linear behavior with the exception of a spike in energy at the same location as the

large cluster of "high" amplitude and "high" frequency hits occurs. Interestingly there is no significant increase in any of the AE features plotted once the onset of strain localization is observed. Fig. 8d shows the location of this localization and its size at the end of the test.
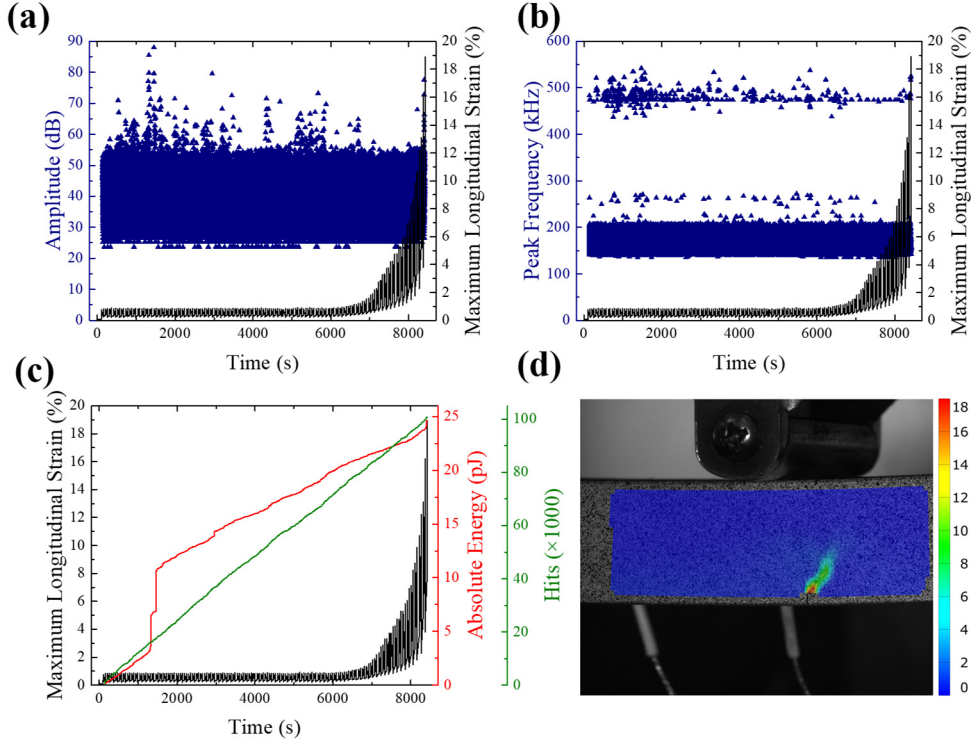

Fig. 8: Acoustic emission features plotted for the entire duration of the fatigue bending test: (a) amplitude, (b) peak frequency, (c) counts, hits, and absolute energy all overlaid with the maximum loading strain, (d) the damage location and size at the end of the test.

Similar to the results in Fig.7, the MSD curve was obtained for the cyclic data of the 3-point bending tests and the results are shown in Fig. 9. Here the damage parameter is plotted with respect to the structure's life fraction where the value of 1 corresponds to the presence of a crack such as the one shown in Fig. 8d.
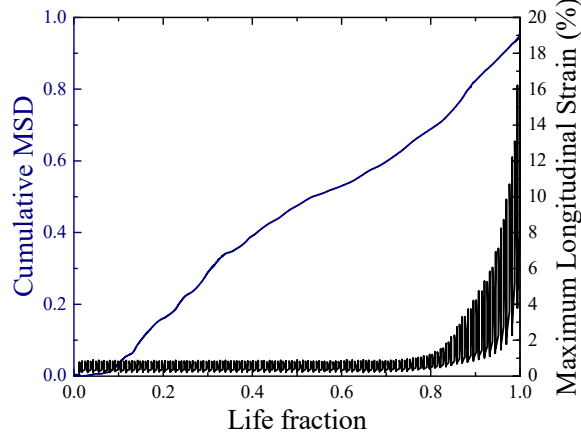
Fig. 9: Normalized cumulative MSD for a 3-point bending beam under cyclic loading.

2.5 Computational approach

The experimental information obtained through the multiphysics experiments and the subsequent outlier analysis was implemented in a computational framework in order to study the damage accumulation trends in specimens of various geometries. Specifically, an isotropic hardening scheme was selected to describe the plasticity effects under monotonic and cyclic conditions in the tensile regime. This was coupled with a continuum local damage law based on stiffness degradation that characterizes void nucleation and growth, and implements the MSD information into the FE domain. To this aim, a user subroutine (UMAT) was developed and the MSD curve previously derived was used in a user hardening (UHARD) subroutine similar to previous work by the authors [57].

The yield function for the isotropic hardening model adopted in this study is given by

$$f = \left(\frac{3}{2} \boldsymbol{\sigma}' : \boldsymbol{\sigma}' \right)^{1/2} - r\left(p\right) - \sigma_y = 0 \ , \tag{2}$$

where $\boldsymbol{\sigma}'$ is the deviatoric stress tensor, $r\left(p\right)$ is the isotropic hardening function, σ_y is the yield stress and p is the equivalent (accumulated) plastic strain, defined as

14

$$p = \int_0^t \dot{p} dt, \qquad \dot{p} = \left(\frac{2}{3} \dot{\boldsymbol{\varepsilon}}^p \dot{\boldsymbol{\varepsilon}}^p \right)^{1/2}, \tag{3}$$

where $\dot{p}$ is the equivalent plastic strain rate and $\dot{\boldsymbol{\varepsilon}}^p$ is the plastic strain rate tensor. Plastic strain increments were determined based on the following plastic flow rule

$$\dot{\boldsymbol{\varepsilon}}^p = \frac{3}{2} \frac{\boldsymbol{\sigma}'}{\sigma_e} \dot{p}, \tag{4}$$

where σ_e is the effective stress, defined as

$$\sigma_e = \left(\frac{3}{2} \boldsymbol{\sigma}' : \boldsymbol{\sigma}' \right)^{1/2}. \tag{5}$$

The elastic strain and stress increments were also determined and all field quantities (stress components, effective plastic strain) were updated at the end of each increment.

Next, a criterion was implemented to initiate the stiffness degradation. Specifically, the total accumulated strain at each integration point of the computational domain was compared to an a priori defined critical value ε_{cr}. If this critical value is reached or exceeded, a stiffness degradation approach was followed. Specifically, for those elements that exhibit a higher accumulated strain at any of their integration points, the corresponding stiffness matrix $\mathbf{C}$ and applied load (stress) $\boldsymbol{\sigma}$ is reduced according to the following relations

$$\mathbf{C} = \left(1 - D \right) \overline{\mathbf{C}}, \qquad \boldsymbol{\sigma} = \left(1 - D \right) \overline{\boldsymbol{\sigma}}, \tag{6}$$

where $\overline{\mathbf{C}}$ is the initial element stiffness, $\overline{\boldsymbol{\sigma}}$ is the effective ('undamaged') stress tensor and D is an overall (scalar) damage variable. The stiffness and load reductions alter the local stress-strain response. The response of the scalar damage parameter D with respect to the applied strain to the tested specimen is shown in Fig. 7. For applied strain up to 0.1, the behavior corresponds to the

elastic regime of the stress-strain curve, and therefore damage accumulation was not considered for this strain range. Stiffness degradation was initiated after yielding and then followed the response of Fig. 7. The damage variable evolution (Fig. 7) was then mathematically approximated as a function of accumulated strain given by the polynomial expression

$$D\left(\varepsilon\right) = 0.0595\varepsilon^6 \cdot 0.35^{2\varepsilon} + 0.48 \cdot 0.35^{\varepsilon} - 0.0102\varepsilon^2 + 0.203\varepsilon - 0.339 \, . \tag{7}$$

Given this development, the computational procedure developed is described as a pseudocode in Fig. 10. This workflow is used to find values of stress, elastic and plastic strain, stiffness components, and damage parameter for every time increment at each integration point in the model.
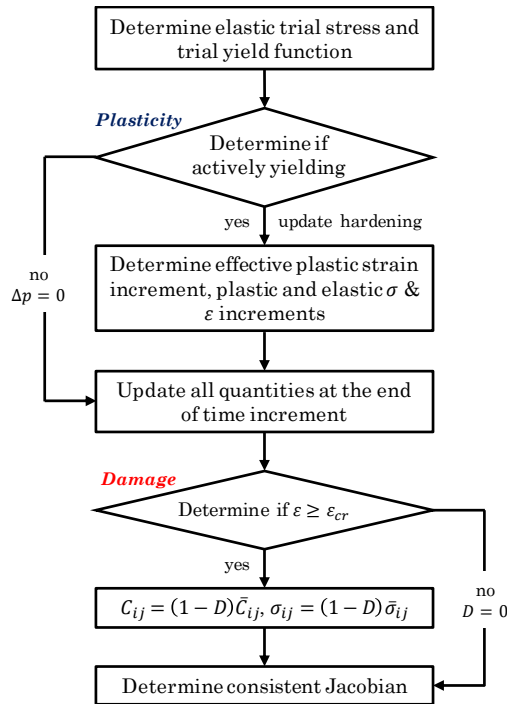

Fig. 10: Pseudocode for implementation of the damage law in a finite element code.

In this study, an implicit integration scheme based on the radial return method was adopted that begins with a selection of a trial stress increment and the determination of a trial yield function.

The trial stress state is compared to a yield criterion, in this case an experimentally defined value of the von Mises stress, and determines if the material is actively yielding. If yielding does not occur $\left(f < 0 \right)$, the algorithm updates all field quantities and returns them to the solver along with the consistent Jacobian. If yielding occurs $\left(f > 0 \right)$, the effective plastic strain increment and the direction and magnitude of the plastic flow were identified through a Newton's iteration scheme. A subroutine (UHARD) was used to calculate the hardening for the current yield state based on tabulated stress-plastic strain experimental data imported into the code (see Fig 7). For the i-th increment, the hardening is evaluated as

$$r^i \left(p \right) = \frac{\sigma_y^i - \sigma_y^{i-1}}{\varepsilon_i^p - \varepsilon_{i-1}^p} \quad , \tag{8}$$

where σ_y^i, ε_i^p and σ_y^{i-1}, ε_{i-1}^p are pairs of yield stress and plastic strain values at the current and previous increments respectively. In the next step, the total strain at any integration point is compared to the damage initiation criterion. If the criterion is met, the current value of the damage variable D is calculated according to Eq. (7) and the element stiffness and load is updated using Eq. (6). If the damage criterion is not yet met, no changes are made to the stiffness or stress tensors. Finally, the material tangent stiffness matrix is calculated and returned to the finite element solver.

This numerical procedure was successfully implemented in ABAQUS [58] as a user subroutine, suitable for both 2D and 3D problems. It is noted that due to the nonlinearities introduced, the problem is either solved statically or dynamically with the aid of (artificial) damping. Two three-dimensional geometrical configurations were used to study the incorporation of this method, a dog-bone specimen under simple tension and a beam under 3-point bending loading. The boundary

17

conditions for both geometries are shown in Fig. 11. The height of the dogbone specimen was 152.54 mm, its thickness equal to 3.18 mm and the reduced section width was 13.54 mm. The top and bottom ends were assumed rigid in accordance with the actual experimental conditions. Hence, the sample was fixed at the top rigid area while displacement was applied at the bottom (Fig. 11a). Accordingly, the beam had a total length of 200 mm, while its width and height were 50 mm and 19 mm respectively. A half longitudinal symmetry model of the beam was used as shown in Fig. 11b. Both models were discretized using structured meshes of linear eight-node brick elements (C3D8). The dogbone model consisted of ~320,000 degrees of freedom (DOF), with an average mesh size of 0.5 mm and the beam comprised ~240,000 DOF in a biased mesh of a minimum size equal to 1 mm (in the center) and 5 mm at the ends.
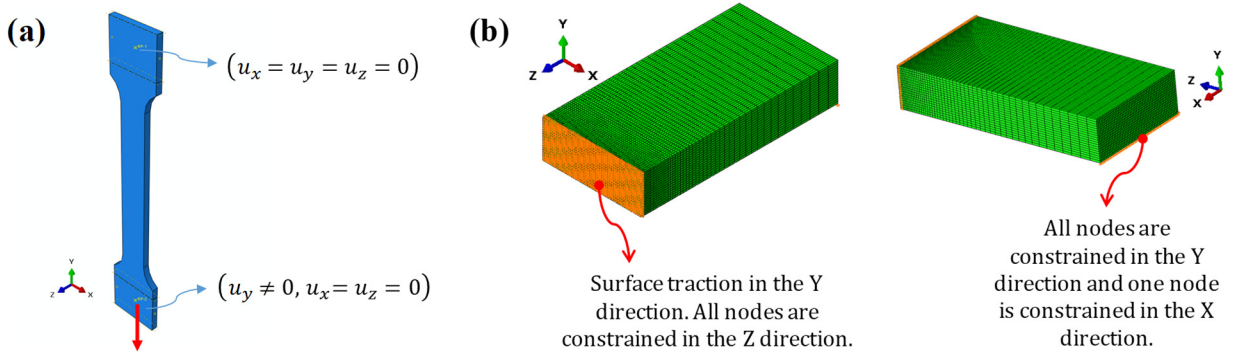

(a)

$(u_x = u_y = u_z = 0)$

$(u_y \neq 0, u_x = u_z = 0)$

(b)

Surface traction in the Y direction. All nodes are constrained in the Z direction.

All nodes are constrained in the Y direction and one node is constrained in the X direction.

Fig. 11: (a) Boundary conditions and loading assignment description for (a) the dogbone coupon and (b) the 3-point bending simulation.

3.   Results and discussion

3.1   *Coupon-level analysis under monotonic and cyclic loading*

The data-driven damage model was first tested on a dogbone specimen subjected to monotonic loading to explore the effect of damage on the bulk mechanical response. Two cases were considered; in the first, the stress-strain response was computed using only an isotropic hardening plasticity scheme, while in the second the stiffness degradation step according to the process described in Fig. 10was added. The results are shown in Fig. 12a, where the "undamaged" and "damaged" designation was adopted to describe the cases without and with the damage model, respectively. Also, the damage parameter output is plotted for the "damaged" case. To obtain the data for these curves, stress and strain values were averaged in a region defined by two parallel lines set at a distance of 10 mm from the midpoint, where deformation localizations were expected to occur. It can be observed that the numerical response of the "undamaged" specimen matches exactly the experimental data, as given in Fig. 5, which was expected as the actual stress-strain curve obtained experimentally was used to define the plasticity in these models.

On the other hand, when the stiffness degradation scheme that incorporates the MSD curve of Fig. 7 was added, the global mechanical behavior was affected significantly. The response follows the undamaged material behavior up to a strain level of $\varepsilon \approx 4.6\%$, after which the stress gradually reduces with further increase in strain. It is worth noting that at an element level, damage initiates at earlier strain stages (after yielding), however, this local effect is not manifested immediately in the macroscopic stress-strain response. The rate of change in the subsequent softening branch follows

the behavior given by the MSD (see Fig. 7), i.e. the damage accumulates at a rapid rate up to $\varepsilon = 12\%$ and then saturates until the ultimate specimen failure.

The same dogbone specimen was also subjected to tension-tension cyclic conditions (using a load ratio of $R = 0.1$) for 15 cycles and the computed stress-strain responses for both undamaged and damaged cases are plotted in Fig. 12b. The undamaged specimen follows the corresponding trend of the monotonic loading case and has generally constant drops in stress at every cycle. A softening effect is noticed after the sixth cycle at $\varepsilon \approx 7.5\%$, which is attributed to significant necking that occurred in the field of view due to large deformations in this model. The response obtained from this simulation can be well compared with other attempts in the literature [see e.g. 59].
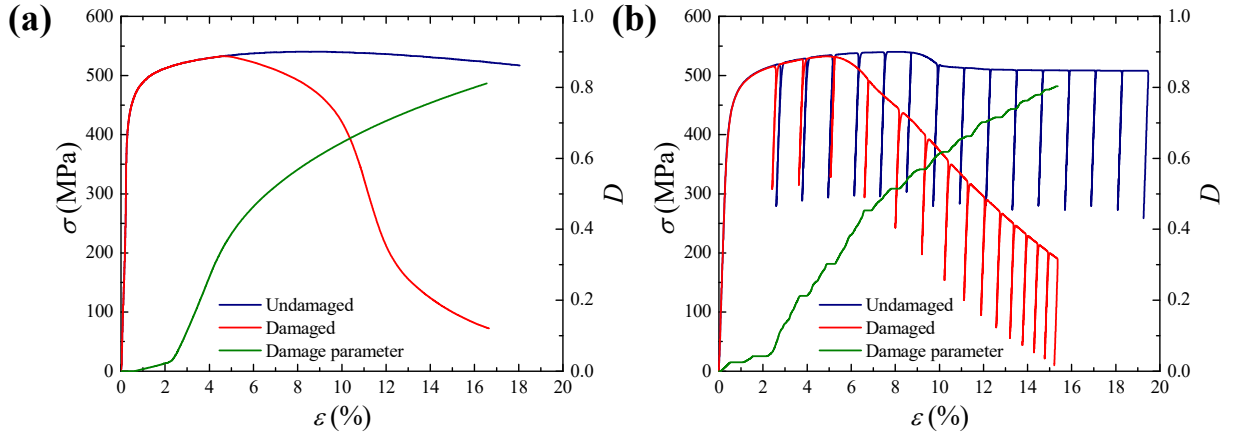

Fig. 12: Stress-strain response and damage parameter output for an undamaged and a damaged specimen following the MSD under (a) monotonic and (b) cyclic loading.

As a comparison, the response of a specimen where the damage curve was added is given in the same graph. The results of this simulation follow the corresponding stress-strain curve of the undamaged specimen for the first three cycles. After an average strain of $\varepsilon \approx 4.8\%$, a softening behavior is obtained since the stress level achieved with further increase in strain are much lower

than that of the undamaged specimen. It is noted that damage initiation is observed at earlier strain stages at a finite element level, as shown in the damage parameter output. After the third loading cycle, a drop of almost constant slope is noticed. The limited capacity of the specimen to undertake load is also noted since after the fourth loading cycle the unloading branches do not coincide with the corresponding ones of the undamaged specimen, i.e. the strain range between cycles is less in this case. As a result, this simulation is concluded at a lower overall strain level. It should be also mentioned that the damage parameter shows a similar trend to the monotonic loading case. A plateau in the damage accumulation is noted at all unloading points.

Moreover, it is worth investigating the effect of the damage model application in the overall deformation mechanism of the specimen. In Fig. 13, full-field results (displacement u_y, Von Mises stress, and strain ε_{yy}) for the undamaged and damaged specimens under monotonic loading are plotted at the same loading stage (the response is similar in the cyclic loading case). In both cases we observe localized deformation around the midpoint of the specimen's height, however, this localization is symmetric in the undamaged specimen case and antisymmetric in the damaged one. In the first case, the deformation mode corresponds to tensile necking, i.e. a reduction of the specimen's cross-sectional area in a small region. On the other hand, the use of a local damage model leads to shear deformation mode, as discussed by the authors [57]. This is mostly evident in the Von Mises stress plot where a diagonal zone of high intensity across the specimen's width is formed. It should be also noted that the localization region is affected by the mesh characteristics (element type, mesh density and discretization type).
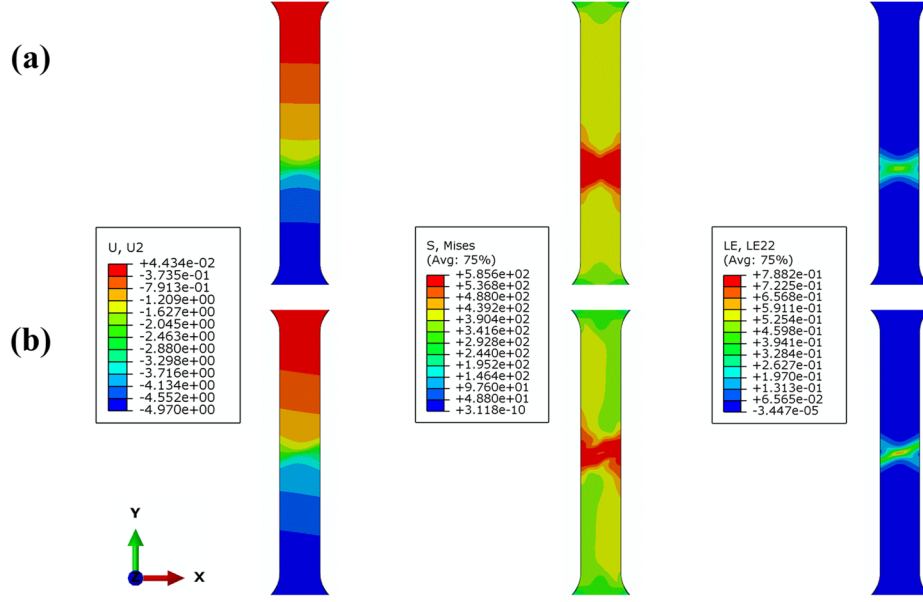
Fig. 13: Comparison of deformation modes between the (a) undamaged and (b) the damaged dogbone specimens under monotonic loading.

3.2 Application to 3-point bending modeling

A beam under 3-point bending loading conditions was investigated next to examine the differences caused by the damage model in this geometry that resembles a structural component. It is reminded that similar to the previous analysis, the experimental information in the form of stress-strain input and damage parameter evolution is applied everywhere in the structure at the element level. Results for monotonic loading conditions are presented in Fig. 14. Specifically, contour plots for the displacement u_y, Von Mises stress, and strain ε_{yy} are given for the case of plasticity (Fig. 14a) and plasticity coupled with damage (Fig. 14b) at the same loading stage. The use of fixed colormaps emphasizes the shift in the response between the two solutions. The maximum beam deflection (at the center) and the normal strain on the y-direction are higher when the damage input is considered while the Von Mises stress is lower as the load carrying capacity of the structure reduces due to damage. A quantitative comparison of the maximum values in the three plots yields a 27% increase

in the vertical displacement, a 23% reduction in the Von Mises stress and an 8% increase in the normal strain, when damage is added in the simulation.
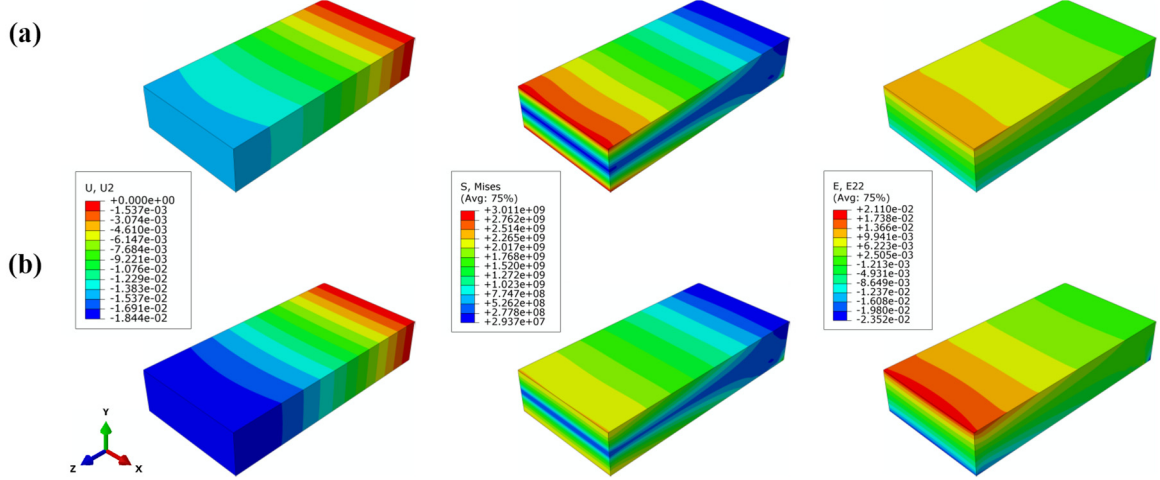

Fig. 14: Full field plots for displacement u_y, Von Mises stress, and strain ε_{yy} for monotonic loading in the case of (a) plasticity and (b) plasticity and damage.

Moreover, the full-field damage evolution at different loading stages is presented in Fig. 15. The damage is accumulated at the center of the beam where the load is applied in a symmetric way with respect to the beam's thickness. The maximum damage value for the four plots are 27%, 52%, 73%, and 100%. In snapshot (d), it is clear that several elements have reached ultimate damage levels. As a reference, it is worth evaluating the ratio of maximum displacement over the displacement at failure (case d) for each of the cases (a) to (c). The corresponding values are 23%, 42%, and 79%.
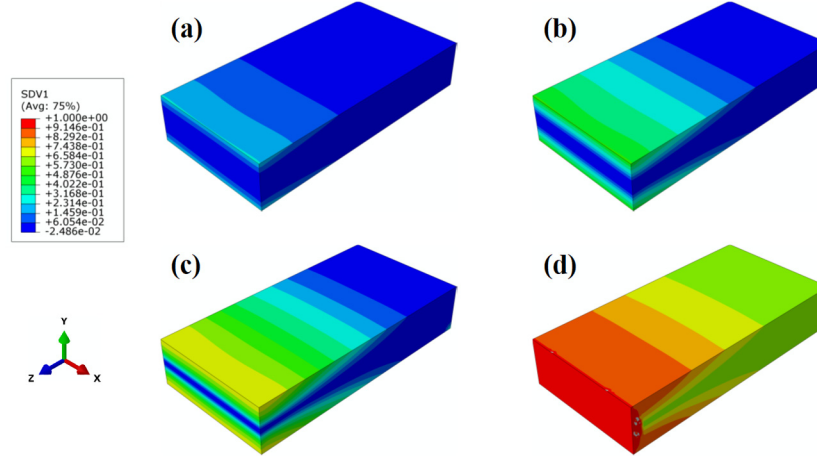
Fig. 15: Damage parameter evolution for monotonic loading. The maximum damage levels are: (a) 27%, (b) 52%, (c) 73%, (d) 100%.

A beam of the same geometry was also studied under (tensile) cyclic 3-point bending loading conditions both using the plasticity law only and employing the stiffness degradation approach. In this series of simulations, the stress amplitude per number of fatigue cycles information (S-N curve) was utilized as extracted from the literature [60] (Fig. 16). A static initial analysis under the maximum load of the given S-N curve was performed first to define the stress at each node of the structure. Using the stress distribution from this analysis, the fatigue life for each integration point was calculated using the S-N diagram. Then, the simulation was run at discrete number of cycles setting the number of loading cycles as a function of computational time. For any given number of cycles, the life fraction was calculated, and the associated value of the damage parameter was introduced in the analysis based on the MSD curve presented in Fig. 9 In this way, the stiffness was degraded at each integration point depending on the loading cycle the analysis was running on.
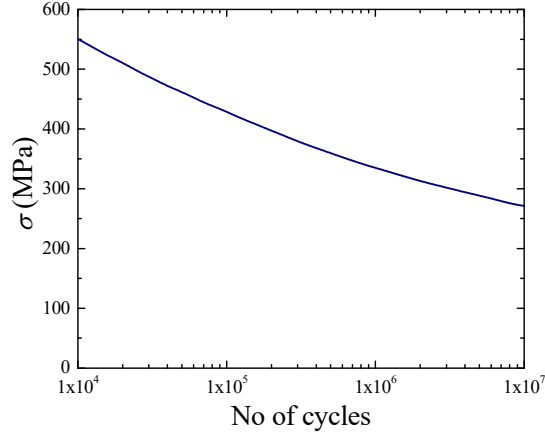
Fig. 16: S-N curve for Al 7075 under tensile cyclic conditions ($R = 0.1$).

The results of this numerical investigation are shown in Fig. 17, which is organized in a similar manner to the monotonic case discussed earlier (see Fig. 14): on the top row full-field plots for the displacement u_y, Von Mises stress, and strain ε_{yy} are given for the case of plasticity only while on the bottom row the same quantities are presented for the case of plasticity coupled with damage, at the same point of fatigue life. Under these loading conditions it is observed that all quantities are significantly increased when damage information is added in the analysis due to the reduction in stiffness. Specifically, the value of the maximum deflection is 1.75 times higher, the maximum Von Mises stress 3.41 times higher, and the normal strain is increased by 4.96 times.

The effect of this increase is further explained in Fig. 18, where the full-field damage evolution (a) and the maximum beam deflection for the two approaches (b) at different stages of fatigue life is shown. The accumulation of damage is already noticed at 1024 cycles while an ultimate failure value is reached in some finite elements at 16,384 cycles. In Fig. 18b, it is shown that the maximum beam deflection remains constant when damage is not incorporated in the model. On the other

hand, the maximum displacement increases significantly with respect to the number of loading cycles. At 4,096 cycles, the values of the two simulations practically coincide, while for 16,384 the increase is 3.84%, for 65,536 cycles 16.4% and for 524,288 cycles 74.5%. Therefore, the degradation of stiffness is essential so as the outcome of the cyclic loading simulation becomes realistic.
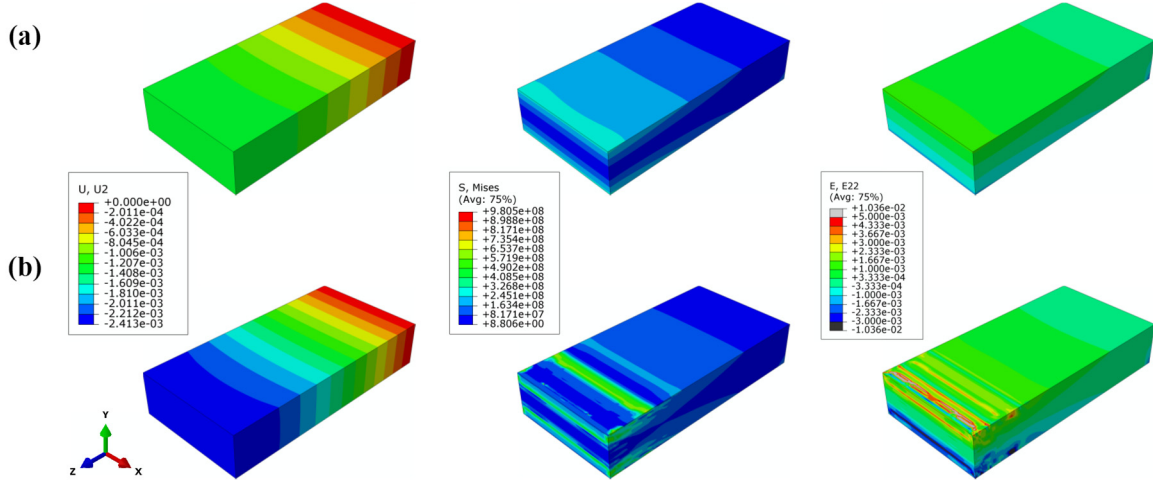

Fig. 17: Full field plots for displacement u_y, Von Mises stress, and strain ε_{yy} for cyclic loading in the case of (a) plasticity and (b) plasticity and damage.
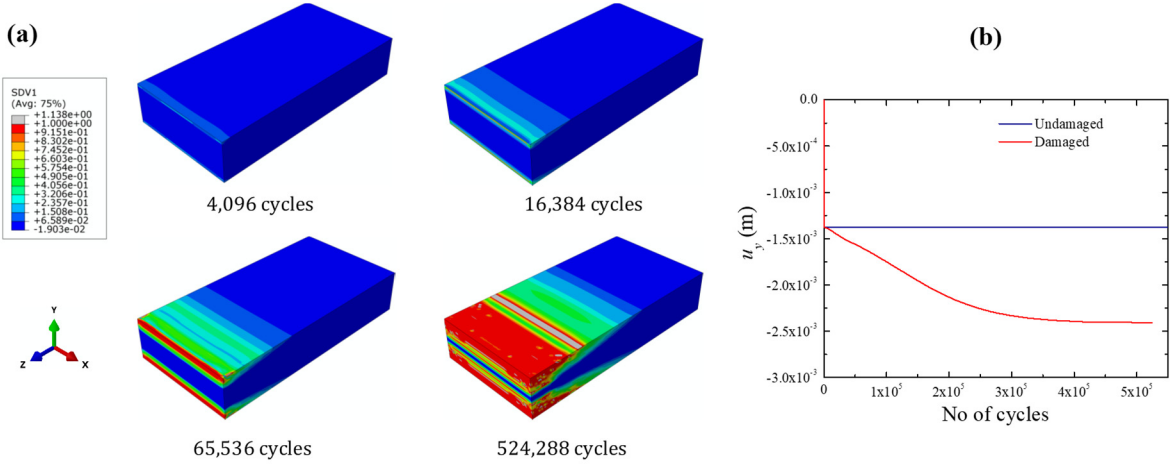

Fig. 18: (a) Damage evolution under cyclic loading, (b) variation of the deflection in the middle of the beam with respect to the number of fatigue cycles using both approaches.

4. Concluding remarks

A data-driven continuum level local damage model based on multiphysics experimental information was proposed in this work. The material was tested inside an SEM and its deformation was monitored using nondestructive acoustic (AE) and optical metrology (DIC) techniques. Data collection was followed by outlier analysis and a microstructurally sensitive damage law was generated. This experimental information was incorporated in numerical models based on custom subroutines implemented in a Finite Element Method that combine a plasticity model with a stiffness degradation approach. Monotonic and cyclic numerical simulations of different geometries were completed in order to study the damage evolution process. The results showed the influence of a microstructure-based damage model in the macroscopic material response. The behavior deviated significantly when compared to analysis based on a macroscopic plasticity law. This effect was emphasized in high-cycle fatigue simulations where the use of a damage model is essential to predict a realistic response. In conclusion, this work contributes to the development of physics-based data-driven damage models that aim to enhance our understanding on material failure and identification of damage precursors.

References

[1] McDowell, D. L., and Dunne, F. P. E., 2010, "Microstructure-sensitive computational modeling of fatigue crack formation," International Journal of Fatigue, 32(9), pp. 1521-1542.

[2] Xue, Y., McDowell, D. L., Horstemeyer, M. F., Dale, M. H., and Jordon, J. B., 2007, "Microstructure-based multistage fatigue modeling of aluminum alloy 7075-T651," Engineering Fracture Mechanics, 74(17), pp. 2810-2823.

[3] Wisner, B., Cabal, M., Vanniamparambil, P. A., Hochhalter, J., Leser, W. P., and Kontsos, A., 2015, "In Situ Microscopic Investigation to Validate Acoustic Emission Monitoring," Experimental Mechanics, 55(9), pp. 1705-1715.

[4] Wisner, B., and Kontsos, A., 2017, "Fatigue Damage Precursor Identification Using Nondestructive Evaluation Coupled with Electron Microscopy," Fracture, Fatigue, Failure and Damage Evolution, Volume 8: Proceedings of the 2016 Annual Conference on Experimental and Applied Mechanics pp. 1-8.

[5] Wisner, B., and Kontsos, A., 2017, "In Situ Monitoring of Particle Fracture in Aluminum Alloys," Fatigue and Fracture of Engineering Materials and Structures, (Accepted).

[6] Yamakov, V., Hochhalter, J. D., Leser, W. P., Warner, J. E., Newman, J. A., Purja Pun, G. P., and Mishin, Y., 2016, "Multiscale modeling of sensory properties of Co–Ni–Al shape memory particles embedded in an Al metal matrix," Journal of Materials Science, 51(3), pp. 1204-1216.

[7] Habtour, E., Cole, D. P., Riddick, J. C., Weiss, V., Robeson, M., Sridharan, R., and Dasgupta, A., 2016, "Detection of fatigue damage precursor using a nonlinear vibration approach," Structural Control and Health Monitoring, 23(12), pp. 1442-1463.

[8] Haile, M. A., Hall, A. J., Yoo, J. H., Coatney, M. D., and Myers, O. J., 2016, "Detection of damage precursors with embedded magnetostrictive particles," Journal of Intelligent Material Systems and Structures, 27(12), pp. 1567-1576.

[9] Hall, A. J., Brennan, I., Raymond, E., Ghoshal, A., Liu, K. C., Coatney, M., Haynes, R., Bradley, N., Weiss, V., and Tzeng, J., 2013, "Damage precursor investigation of fiber-reinforced composite

materials under fatigue loads," ARMY RESEARCH LAB ABERDEEN PROVING GROUND MD VEHICLE TECHNOLOGY DIRECTORATE.

[10] Weiss, V., and Ghoshal, A., 2014, "On the search for optimal damage precursors," Structural Health Monitoring, 13(6), pp. 601-608.

[11] Lemaitre, J., and Desmorat, R., 2005, Engineering damage mechanics: ductile, creep, fatigue and brittle failures, Springer Science & Business Media.

[12] Kuna, M., and Wippler, S., 2010, "A cyclic viscoplastic and creep damage model for lead free solder alloys," Engineering Fracture Mechanics, 77(18), pp. 3635-3647.

[13] Richard, B., Ragueneau, F., Cremona, C., and Adelaide, L., 2010, "Isotropic continuum damage mechanics for concrete under cyclic loading: Stiffness recovery, inelastic strains and frictional sliding," Engineering Fracture Mechanics, 77(8), pp. 1203-1223.

[14] Liu, P. F., and Zheng, J. Y., 2010, "Recent developments on damage modeling and finite element analysis for composite laminates: A review," Materials & Design, 31(8), pp. 3825-3834.

[15] Rinaldi, A., Krajcinovic, D., and Mastilovic, S., 2006, Statistical damage mechanics – constitutive relations.

[16] Abanto-Bueno, J., and Lambros, J., 2002, "Investigation of crack growth in functionally graded materials using digital image correlation," Engineering Fracture Mechanics, 69(14), pp. 1695-1711.

[17] Chan, K. S., 2010, "Roles of microstructure in fatigue crack initiation," International Journal of Fatigue, 32(9), pp. 1428-1447.

[18] Dunegan, H., Harris, D., and Tetelman, A., "Detection of fatigue crack growth by acoustic emission techniques," Proc. pp 20-31 of Proceedings of the Seventh Symposium on Nondestructive Evaluation of Components and Materials in Aerospace, Weapons Systems, and Nuclear Applications, April 23--25, 1969, San Antonio, Texa, Univ. of California, Livermore.

[19] Hazeli, K., Askari, H., Cuadra, J., Streller, F., Carpick, R. W., Zbib, H. M., and Kontsos, A., 2015, "Microstructure-sensitive investigation of magnesium alloy fatigue," International Journal of Plasticity, 68, pp. 55-76.

[20] Miao, J., Pollock, T. M., and Wayne Jones, J., 2009, "Crystallographic fatigue crack initiation in nickel-based superalloy René 88DT at elevated temperature," Acta Materialia, 57(20), pp. 5964-5974.

[21] Zhang, W., and Liu, Y., 2012, "In situ SEM testing for crack closure investigation and virtual crack annealing model development," International Journal of Fatigue, 43, pp. 188-196.

[22] Zhong, Z., Ai, X., Liu, Z., Liu, J., and Xu, Q., 2015, "Surface morphology and microcrack formation for 7050-T7451 aluminum alloy in high speed milling," The International Journal of Advanced Manufacturing Technology, 78(1), pp. 281-296.

[23] Rajaram, S., Vanniamparambil, P. A., Khan, F., Bolhassani, M., Koutras, A., Bartoli, I., Moon, F., Hamid, A., Benson Shing, P., Tyson, J., and Kontsos, A., 2017, "Full-field deformation measurements during seismic loading of masonry buildings," Structural Control and Health Monitoring, 24(4), pp. e1903-n/a.

[24] Vanniamparambil, P. A., Cuadra, J., Guclu, U., Bartoli, I., and Kontsos, A., "Cross-validated detection of crack initiation in aerospace materials," Proc. SPIE Smart Structures and Materials+ Nondestructive Evaluation and Health Monitoring, International Society for Optics and Photonics, pp. 906429-906429-906411.

[25] Payne, J., Welsh, G., Christ, R. J., Nardiello, J., and Papazian, J. M., 2010, "Observations of fatigue crack initiation in 7075-T651," International Journal of Fatigue, 32(2), pp. 247-255.

[26] Bozek, J., Hochhalter, J., Veilleux, M., Liu, M., Heber, G., Sintay, S., Rollett, A., Littlewood, D., Maniatty, A., and Weiland, H., 2008, "A geometric approach to modeling microstructurally small fatigue crack formation: I. Probabilistic simulation of constituent particle cracking in AA 7075-T651," Modelling and Simulation in Materials Science and Engineering, 16(6), p. 065007.

[27] Vanniamparambil, P. A., Guclu, U., and Kontsos, A., 2015, "Identification of Crack Initiation in Aluminum Alloys using Acoustic Emission," Experimental Mechanics, 55(5), pp. 837-850.

[28] Hazeli, K., Cuadra, J., Streller, F., Barr, C. M., Taheri, M. L., Carpick, R. W., and Kontsos, A., 2015, "Three-dimensional effects of twinning in magnesium alloys," Scripta Materialia, 100, pp. 9-12.

[29] Hazeli, K., Cuadra, J., Vanniamparambil, P. A., and Kontsos, A., 2013, "In situ identification of twin-related bands near yielding in a magnesium alloy," Scripta Materialia, 68(1), pp. 83-86.

[30] Mo, C., Wisner, B., Cabal, M., Hazeli, K., Ramesh, K., El Kadiri, H., Al-Samman, T., Molodov, K., Molodov, D., and Kontsos, A., 2016, "Acoustic Emission of Deformation Twinning in Magnesium," Materials, 9(8), p. 662.

[31] Carroll, J. D., Abuzaid, W., Lambros, J., and Sehitoglu, H., 2013, "High resolution digital image correlation measurements of strain accumulation in fatigue crack growth," International Journal of Fatigue, 57, pp. 140-150.

[32] Kammers, A., and Daly, S., 2011, "Small-scale patterning methods for digital image correlation under scanning electron microscopy," Measurement Science and Technology, 22(12), p. 125501.

[33] Kammers, A. D., and Daly, S., 2013, "Digital Image Correlation under Scanning Electron Microscopy: Methodology and Validation," Experimental Mechanics, 53(9), pp. 1743-1761.

[34] Bianchetti, R., Hamstad, M., and Mukherjee, A., 1976, "Origin of Burst-Type Acoustic Emission in Unflawed 7075-T6 Aluminum."

[35] Frederick, J., and Felbeck, D., 1972, "Dislocation motion as a source of acoustic emission," Acoustic Emission, ASTM International.

[36] Baram, J., and Rosen, M., 1979, "Acoustic emission generated during the tensile testing of aluminium alloys," Materials Science and Engineering, 40(1), pp. 21-29.

[37] Carmi, R., Vanniamparambil, P. A., Cuadra, J., Hazeli, K., Rajaram, S., Guclu, U., Bussiba, A., Bartoli, I., and Kontsos, A., 2015, "Acoustic Emission and Digital Image Correlation as Complementary Techniques for Laboratory and Field Research," Advances in Acoustic Emission Technology: Proceedings of the World Conference on Acoustic Emission–2013, G. Shen, Z. Wu, and J. Zhang, eds., Springer New York, New York, NY, pp. 605-622.

[38] Cousland, S. M., and Scala, C. M., 1983, "Acoustic emission during the plastic deformation of aluminium alloys 2024 and 2124," Materials Science and Engineering, 57(1), pp. 23-29.

[39] Roberts, T. M., and Talebzadeh, M., 2003, "Acoustic emission monitoring of fatigue crack propagation," Journal of Constructional Steel Research, 59(6), pp. 695-712.

[40] Vanniamparambil, P. A., Bartoli, I., Hazeli, K., Cuadra, J., Schwartz, E., Saralaya, R., and Kontsos, A., 2012, "An integrated structural health monitoring approach for crack growth monitoring," Journal of Intelligent Material Systems and Structures, 23(14), pp. 1563-1573.

[41] Iziumova, A., and Plekhov, O., 2014, "Calculation of the energy J-integral in plastic zone ahead of a crack tip by infrared scanning," Fatigue & Fracture of Engineering Materials & Structures, 37(12), pp. 1330-1337.

[42] Plekhov, O., Palin-Luc, T., Saintier, N., Uvarov, S., and Naimark, O., 2005, "Fatigue crack initiation and growth in a 35CrMo4 steel investigated by infrared thermography," Fatigue & Fracture of Engineering Materials & Structures, 28(1-2), pp. 169-178.

[43] Wagner, D., Ranc, N., Bathias, C., and Paris, P. C., 2010, "Fatigue crack initiation detection by an infrared thermography method," Fatigue & Fracture of Engineering Materials & Structures, 33(1), pp. 12-21.

[44] Ayres, J. W., Lalande, F., Chaudhry, Z., and Rogers, C. A., 1998, "Qualitative impedance-based health monitoring of civil infrastructures," Smart Materials and Structures, 7(5), p. 599.

[45] Lim, Y. Y., and Soh, C. K., 2011, "Fatigue life estimation of a 1D aluminum beam under mode-I loading using theelectromechanical impedance technique," Smart Materials and Structures, 20(12), p. 125001.

[46] Park, G., Cudney Harley, H., and Inman Daniel, J., 2000, "Impedance-Based Health Monitoring of Civil Structural Components," Journal of Infrastructure Systems, 6(4), pp. 153-160.

[47] Finlayson, R. D., Friesel, M., Carlos, M., Cole, P., and Lenain, J., 2001, "Health monitoring of aerospace structures with acoustic emission and acousto-ultrasonics," Insight, 43(3), pp. 155-158.

[48] Saka, M., and Uchikawa, T., 1995, "Simplified NDE of a closed vertical crack using ultrasonics," NDT & E International, 28(5), pp. 289-296.

[49] Tittmann, B. R., and Buck, O., 1980, "Fatigue lifetime prediction with the aid of SAW NDE," Journal of Nondestructive Evaluation, 1(2), pp. 123-136.

[50] Barbero, E. J., Abdelal, G. F., and Caceres, A., 2005, "A micromechanics approach for damage modeling of polymer matrix composites," Composite Structures, 67(4), pp. 427-436.

[51] Kompalka, A. S., Reese, S., and Bruhns, O. T., 2007, "Experimental investigation of damage evolution by data-driven stochastic subspace identification and iterative finite element model updating," Archive of Applied Mechanics, 77(8), pp. 559-573.

[52] Zárate, B., A., Caicedo, J., M., Yu, J., and Ziehl, P., 2012, "Probabilistic Prognosis of Fatigue Crack Growth Using Acoustic Emission Data," Journal of Engineering Mechanics, 138(9), pp. 1101-1111.

[53] Loutas, T., Eleftheroglou, N., and Zarouchas, D., 2017, "A data-driven probabilistic framework towards the in-situ prognostics of fatigue life of composites based on acoustic emission data," Composite Structures, 161, pp. 522-529.

[54] Davis, J., "ASM Specialty Handbook: Aluminum and Aluminum Alloys, 1993," ASM International, Materials Park, OH, USA.

[55] Merati, A., 2005, "A study of nucleation and fatigue behavior of an aerospace aluminum alloy 2024-T3," International Journal of Fatigue, 27(1), pp. 33-44.

[56] Xue, Y., El Kadiri, H., Horstemeyer, M. F., Jordon, J. B., and Weiland, H., 2007, "Micromechanisms of multistage fatigue crack growth in a high-strength aluminum alloy," Acta Materialia, 55(6), pp. 1975-1984.

[57] Baxevanakis, K. P., Mo, C., Cabal, M., and Kontsos, A., 2017, "An integrated approach to model strain localization bands in magnesium alloys," Computational Mechanics, (Available Online).

[58] ABAQUS, 2013, version 6.13, 2013. User's Manual. Dassault Systems, Pawtucket, RI.

[59] Wang, Y., and Wang, Z., 2016, "Experimental Investigation and FE Analysis on Constitutive Relationship of High Strength Aluminum Alloy under Cyclic Loading," Advances in Materials Science and Engineering, 2016, p. 16.

[60] Liu, A. F., 2005, Mechanics and mechanisms of fracture: an introduction, ASM International.